Available online at www.sciencedirect.com
SCIENCE DIRECT
Journal of Power Sources 146 (2005) 630–635
JOURNAL OF POWER SOURCES
www.elsevier.com/locate/jpowsour

Structural and electrochemical characterization of $Li[(CoNi_{1/2}Mn_{1/2})_x(Li_{1/3}Mn_{2/3})_{(1-2x)}]O_2$ solid solutions with layered lithium manganese oxides

S.J. Jin, K.S. Park, C.H. Song, M.H. Cho, K.S. Nahm*, Y.B. Hahn, Y.S. Lee

School of Chemical Engineering & Technology, Chonbuk National University, Jeonju 561-756, Republic of Korea

Available online 1 June 2005

Abstract

Five compositions of $Li[(CoNi_{1/2}Mn_{1/2})_x(Li_{1/3}Mn_{2/3})_{(1-2x)}]O_2$ solid solutions with layered lithium manganese oxides were designed using a triangle phase diagram and were synthesized using a sol–gel method. The phase diagram satisfied the theoretical manganese oxidation state of 4+ over the whole triangle plane of the diagram and was expressed with a design equation of $Li[(CoNi_{1/2}Mn_{1/2})_x(Li_{1/3}Mn_{2/3})_{(1-2x)}]O_2$. It was found that the solid solutions were synthesized with layered structure maintaining the manganese oxidation state of 4+ and showed a one-step monotonous discharge curve shape without structural transformation to spinel during charge/discharge processes. The synthesized solid solutions delivered high discharge capacities with negligible capacity fading.

Keywords: Phase diagram; Solid solutions; Layered structure; Cathode materials; Lithium batteries

1. Introduction

Layered lithium manganese oxides are attractive cathode materials for lithium secondary batteries because of various advantages over conventional $LiCoO_2$ cathode material [1,2]. In recent, many researchers have focused on the preparation of solid solutions with layered lithium manganese oxides, which maintain Mn^{4+} with stable layered structure [5–11]. Based on experimental observations, they proposed various design equations, such as $Li_xMn_yNi_{1-y}O_2$ [3], $Li[Li_{(1-2x)/3}Ni_xMn_{(2-x)/3}]O_2$ [4], $Li[Mn_xNi_x(Li_{1/3}Mn_{2/3})_{1-2x}]O_2$ [5,6], $Li[Ni_xLi_{(1/3-2x/3)}Mn_{(2/3-x/3)}]O_2$ [7], $Li[Ni_xMn_xCo_{1-2x}]O_2$, $Li[Li_{0.2}Cr_{0.4}Mn_{0.4}]O_2$ [8], $Li[Ni_xMn_xCo_{1-2x}]O_2$ [9], and $Li[Ni_xMn_xCo_{1-2x}]O_2$ [10]. Summarizing their works, the solid solutions synthesized using the proposed design equations had typical rhombohedral structure (S.G.: $R\bar{3}m$) showed a monotonous charge/discharge curves without the change of Mn oxidation state during charge/discharge processes. Ammundsen et al. [8] attempted to express the solid solutions on two triangle phase diagrams of $LiMnO_2$–$LiNiO_2$–Li_2MnO_3 and $LiMnO_2$–$LiCrO_2$–Li_2MnO_3 systems. But all the compositions of the solid solutions cannot be unanimously depicted on the derived phase diagrams.

In this work, we developed a new triangle phase diagram for expressing all the compositions of solid solutions so far reported. The phase diagram was designed to satisfy the theoretical manganese oxidation state of 4+ in layered manganese oxides solid solutions. To examine if the triangle phase diagram is reliably applicable for designing new manganese oxides solid solutions, five compositions of the solid solutions were randomly chosen from the phase diagram and synthesized using a sol–gel method. The structural and electrochemical characterization was performed for the synthesized solid solutions.

2. Experiment

$Li[(CoNi_{1/2}Mn_{1/2})_x(Li_{1/3}Mn_{2/3})_{(1-2x)}]O_2$ precursor was synthesized using a sol–gel method. Stoichiometric

* Corresponding author. Tel.: +82 63 270 2311; fax: +82 63 270 2306.
E-mail address: nahmks@chonbuk.ac.kr (K.S. Nahm).

0378-7753/$ – see front matter © 2005 Elsevier B.V. All rights reserved.
doi:10.1016/j.jpowsour.2005.03.167

amounts of lithium acetate ($CH_3COOLi{\cdot}2H_2O$), nickel acetate ($(CH_3COO)_2Ni{\cdot}4H_2O$), manganese acetate ($(CH_3COO)_2Mn{\cdot}4H_2O$), and cobalt acetate ($(CH_3COO)_2Co$) were dissolved in deionized water. The dissolved solution was added drop by drop into a continuously agitating aqueous glycolic acid. The pH of the solution was in the range of 5–5.5. The prepared solution was evaporated at 70–80 °C. The resulting gel precursors were heated with a ramping rate of 1 °C min^{-1} and decomposed at 450 °C for 10 h in air. Thus, obtained powders were calcined for 10 h at the temperature range of 950 °C in atmosphere.

The structure of the prepared powders was characterized using X-ray diffraction (XRD) and scanning electron microscopy (SEM). The electrochemical characterization was carried out using CR2032 coin-type cells. A cathode was fabricated with active material (20 mg) and conductive binder (13 mg). It was pressed on 25 mm^2 stainless steel mesh current collector at 300 kg cm^{-2} and dried at 200 °C for 5 h in an oven. The cell was composed of the cathode and a lithium metal anode (Cyprus Foote Mineral Co.) separated by a porous polypropylene film separator (Celgard 3401). The electrolyte was a 1 M $LiPF_6$–ethylene carbonate (EC)/dimethyl carbonate (DMC) (1:2, v/v). The cells were assembled in an argon-filled dry box and tested at room temperature. The cell was charged and discharged at a current density of 0.4 mA cm^{-2} (20 mAh g^{-1}) with cut-off voltages from 2.5 V to an upper voltage of 4.5 V (versus Li/Li$^+$).

3. Results and discussion

Two rules were proposed to synthesize solid solutions with Mn^{4+} [11]. The first rule was that the sum of metal cations occupying on the 3b sites of space group $R\bar{3}m$ (1 6 6) in the transition metal layers is to be one. The second rule was that the sum of the products of the composition and oxidation state of each metal cation in the transition metal layers must be three. The first rule is the condition to make the stoichiometry to be one and the second rule the condition to make the manganese oxidation state to be 4+. Fig. 1 shows new phase diagram consisting of $Li[Ni_{1/2}Mn_{1/2}]O_2$, $LiCoO_2$, and Li_2MnO_3 presented by based on the rules. The detailed design of the phase diagram was discussed in out previous report [12]. The calculated theoretical manganese oxidation states are all four over the whole triangle plane.

From the phase diagram, we randomly chose five compositions along a line expressed with a design equation of $Li[(CoNi_{1/2}Mn_{1/2})_x(Li_{1/3}Mn_{2/3})_{(1-2x)}]O_2$ and synthesized them using a sol–gel method. The synthesized samples are $Li[Li_{4/15}Ni_{1/20}Co_{1/10}Mn_{7/12}]O_2$ ($x = 0.1$) (sample A), $Li[Li_{1/5}Ni_{1/10}Co_{1/5}Mn_{1/2}]O_2$ ($x = 0.2$) (sample B), $Li[Li_{2/15}Ni_{3/20}Co_{3/10}Mn_{5/12}]O_2$ ($x = 0.3$) (sample C), $Li[Li_{1/15}Ni_{1/5}Co_{2/5}Mn_{1/3}]O_2$ ($x = 0.4$) (sample D), and $Li[Ni_{1/4}Co_{1/2}Mn_{1/4}]O2$ ($x = 0.5$) (sample E), marked with five points (a–e) in Fig. 1, respectively.

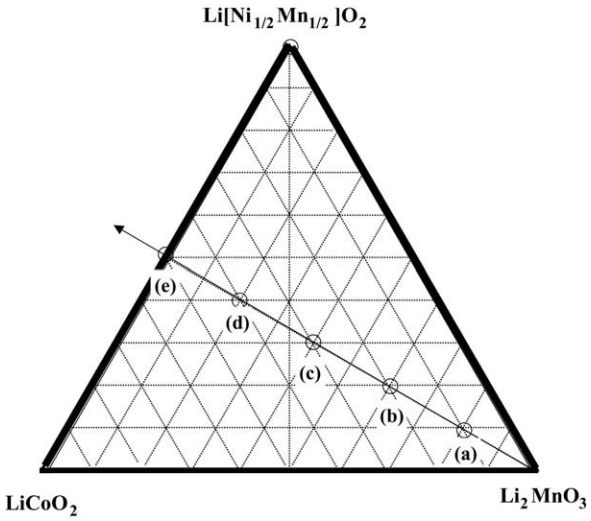

Fig. 1. A new triangle phase diagram of $LiNi_{1/2}Mn_{1/2}O_2$–$LiCoO_2$–Li_2MnO_3 system. The design equation of the phase diagram is $Li[(CoNi_{1/2}Mn_{1/2})_x(Li_{1/3}Mn_{2/3})_{(1-2x)}]O_2$. The points a–e on the triangle plane represent compositions of sample A: ($Li[Li_{4/15}Ni_{1/20}Co_{1/10}Mn_{7/12}]O_2$), sample B: ($Li[Li_{1/5}Ni_{1/10}Co_{1/5}Mn_{1/2}]O_2$), sample C: ($Li[Li_{2/15}Ni_{3/20}Co_{3/10}Mn_{5/12}]O_2$), sample D: ($Li[Li_{1/15}Ni_{1/5}Co_{2/5}Mn_{1/3}]O_2$), and sample E: ($Li[Ni_{1/4}Co_{1/2}Mn_{1/4}]O_2$).

Fig. 2 shows the XRD patterns for the $Li[(CoNi_{1/2}Mn_{1/2})_x(Li_{1/3}Mn_{2/3})_{(1-2x)}]O_2$ samples with Miller indices for each peak. As-prepared samples are all indexed by assuming a layer manganese oxide structure based on a hexagonal α-$NaFeO_2$ structure (space group $R\bar{3}m$ (1 6 6)). All the samples show a (0 0 3) peak at $2\theta = 18°$ as a main peak. The (1 0 4), (1 0 1), (0 0 6), (0 1 2), (0 1 8), and (1 1 0) planes are also observed at $2\theta = 45°$, 37°, 38°, 38.5°, 54.5°, and 65.5°, respectively. The structural characterization clearly demonstrates that the synthesized solid solutions are synthesized

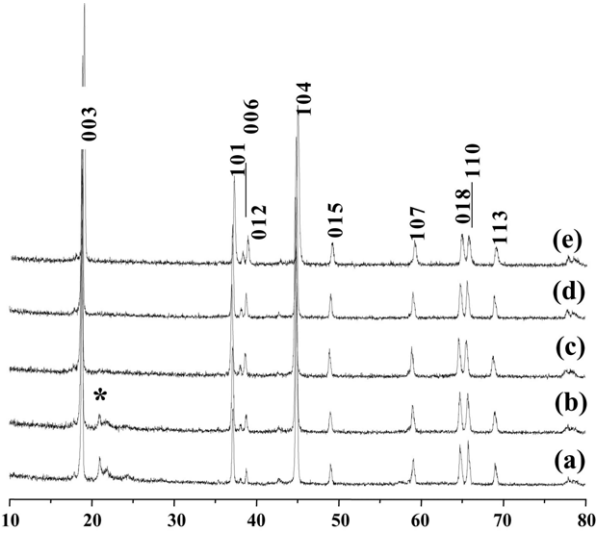

Fig. 2. XRD patterns for the synthesized $Li[(CoNi_{1/2}Mn_{1/2})_x(Li_{1/3}Mn_{2/3})_{(1-2x)}]O_2$. (a) Sample A, (b) sample B, (c) sample C, (d) sample D, and (e) sample E.

with typical layered structure. The appearance of the broad peaks between 20° and 25° from samples A and B is due to the formation of Li_2MnO_3 phase. The superlattice peaks result from the short-range ordering of Li, Ni, Co, and Mn atoms in the transition metal layers as an impurity peak. However, the superlattice peaks are not observed from samples C–E and gradually disappear from sample position (a–e).

EDX spectra measured from regions marked over FE-SEM pictures of samples A, C, and E, respectively, are shown in shown in Fig. 3a–c. The particles size of samples is between 400 and 500 nm with uniform distribution. The EDX spectra show that both samples are composed of Ni, Co, Mn, and O species, but Li ion is not detected due to low energy density. Molar ratio of each chemical species was calculated by dividing moles of each species with moles of Ni, measured from EDX data. The calculated molar ratios of Ni, Co, Mn, and O for the synthesized materials are listed in table in figure, together with those for starting stoichiometric materials. The calculated values are almost same for both the samples before and after the synthesis. It means that the actual stoichiometry of the samples is very close to the target value.

Fig. 4 shows plots of discharge capacity versus cycle number measured at room temperature for Li/$LiPF_6$–EC/DMC (1:2, v/v)/$Li[(CoNi_{1/2}Mn_{1/2})_x(Li_{1/3}Mn_{2/3})_{(1-2x)}]O_2$ electrodes. Typical discharge capacities versus voltage curves are shown for samples B and E in inset. All the synthesized $Li[(CoNi_{1/2}Mn_{1/2})_x(Li_{1/3}Mn_{2/3})_{(1-2x)}]O_2$ materials produce monotonous discharge curves with one step, which are observed from typical layered manganese oxides solid solutions. The discharge capacities of samples A–E are 96, 190, 184, 154, and 183 mAh g^{-1}, respectively, at the first cycle and gradually vary with the cycle number to be subsequently 219, 229, 180, 153, and 169 mAh g^{-1}, respectively, after 40th cycle. The capacity fading ratios for maximum capacities of samples A–E are 0, 0.032, 0.054, 0.016, and 0.19% $cycle^{-1}$, respectively. Low discharge capacity fading indicates that the $Li[(CoNi_{1/2}Mn_{1/2})_x(Li_{1/3}Mn_{2/3})_{(1-2x)}]O_2$ solid solutions are not undergone structural transformation during the cycling since they are synthesized with a stable layered structure. The above results demonstrate that the phase diagram and the design equation employed in this work can be useful to prepare layered lithium manganese oxides solid solutions with a stable layered structure.

It is interesting to see that the discharge capacities of samples A and B gradually increase with the cycle number to reach a maximum capacity, but other samples do not. In addition, samples A and B retain higher discharge capacities than other samples, with a negligible capacity fading. These were frequently observed from layered manganese oxides solid solutions in which Li ion inserts on the transition metal layer [4–6,13]. The layered sold solutions showed that the discharge capacity steadily increases with cycling at initial cycle numbers to reach a maximum capacity, and further cycling decreases the capacity slowly. Kim and Sun explained this is due to the stabilization of the Mn oxides

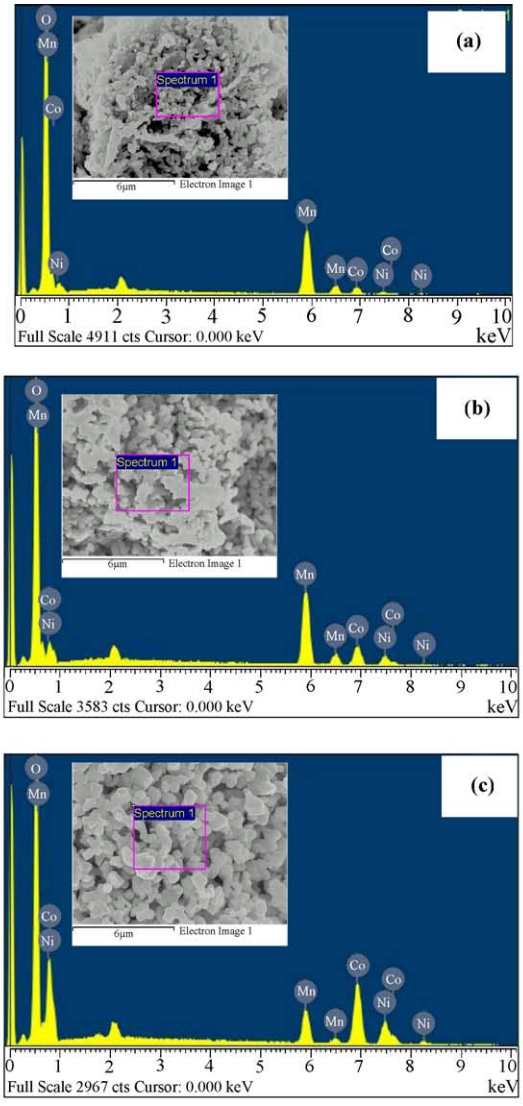

	Sample A		Sample C		Sample E	
	T. R	E.R	T. R	E.R	T. R	E.R
O	40	38	20	18.6	8	7.8
Mn	12	12	5	4.4	1	0.8
Co	2	2	2	1.9	2	1.9
Ni	1	1	1	1	1	1

***T.R: Theoretical ratio, *E.R: Experimental retio**

Fig. 3. FE-SEM images for samples A, B, and E with their corresponding EDX spectra and compositions.

with cycling [13]. The insertion and extraction of Li ions at higher current densities might progressively stabilize as-prepared oxides with cycling to form a stable structure. Meanwhile, it was also explained that the increase of the initial discharge capacity and higher capacity could be because the oxidation state of Mn could be changed from 4+ to 3+ (for discharge process) or from 3+ to 4+ (for charge process)

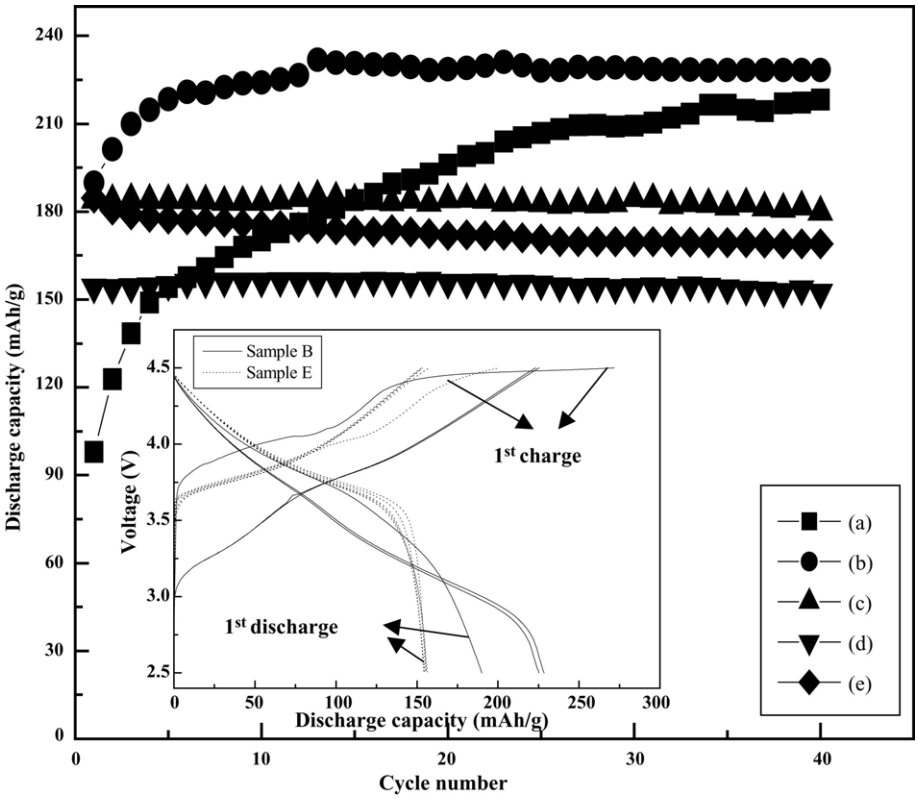

Fig. 4. Discharge capacity vs. cycle number for samples A–E. Typical Capacity vs. voltage curves for samples B and E are inserted in the figure.

during cycling [13,14]. However, it is not clearly understood why the capacity increases with increasing cycles.

We measured dQ/dV for samples A–C with varying applied voltage. Fig. 5a–c shows dQ/dV curves versus voltage between 2.5 and 4.5 V for the samples A–C, respectively. The samples A–C show a similar behavior above 3.5 V. All the samples produce two peaks though they appear at slightly different positions. The two peaks appear at 4.10 and 4.48 V, 3.79 and 4.46 V, and 3.77 and 4.49 V, for samples A–C, respectively, during the first charge process. During the first discharge process, samples A and C show only one peak at 4.07 and 3.75 V, respectively, but sample B exhibits two peaks at 3.41 and 3.79 V, respectively. In the second charge process, the sample B raises a new peak at 3.26 V and the peak observed at 3.97 V shifts to 3.74 V. Meanwhile, the peaks observed at 4.46 and 4.49 V almost disappear in samples B and C, but the peak observed at 4.48 V fades gradually with cycling in sample A. After the first cycle, the dQ/dV curves of samples B and C show almost same behavior for all the other cycles. For sample A, a new peak appears at 3.25 V in the second discharge process and grows until 35 cycles. The increased cycle numbers also show the appearance of a new peak in the charge process, as observed from sample B.

From the first charge process, the peaks observed between 3.7 and 4.1 V in the first charge process are due to the oxidation of Ni^{2+} to Ni^{4+} in the material [15]. But the oxidation peak of Mn^{3+} to Mn^{4+}, which arises below 3.5 V [16], is not observed in the process. This partially proves that as-prepared samples were synthesized with Mn^{4+}. In the first charge process, the Ni^{2+} is oxidized to Ni^{4+}, but Mn remains in the 4+ oxidation state [15,17]. The drastically grown oxidation peak above 4.46 V is due to an irreversible capacity. The peak rises due to electrons removed from oxygen atoms in the structure of the cathode material at higher applied voltage, which results in a partial loss of oxygen from the electrode [15,17]. This peak abruptly disappears in the samples B and C after the first cycle, whereas it gradually decreases in the sample A. In the first discharge process, all the samples show the reduction peak of Ni^{4+} to Ni^{2+} although the peak position is slightly different. Samples A and C exhibit only the reduction peak of nickel, but the reduction peak of Mn^{4+} to Mn^{3+} is observed at 3.3 V together with that of nickel from sample B.

In the second charge process, the oxidation peak of Mn^{3+}/Mn^{4+} begins to grow below 3.5 V, together with that of Ni^{2+}/Ni^{4+} from sample B. With increasing cycle number, sample A also produces both the oxidation peaks of manganese and nickel though the growth rate of the manganese oxidation peak is slower than that of sample B. The oxidation peak of manganese grows with cycling, whereas that of nickel unchanged, though the saturation times for the peak growth are different for samples A and B, respectively. The growth of the manganese oxidation peak is rapidly saturated

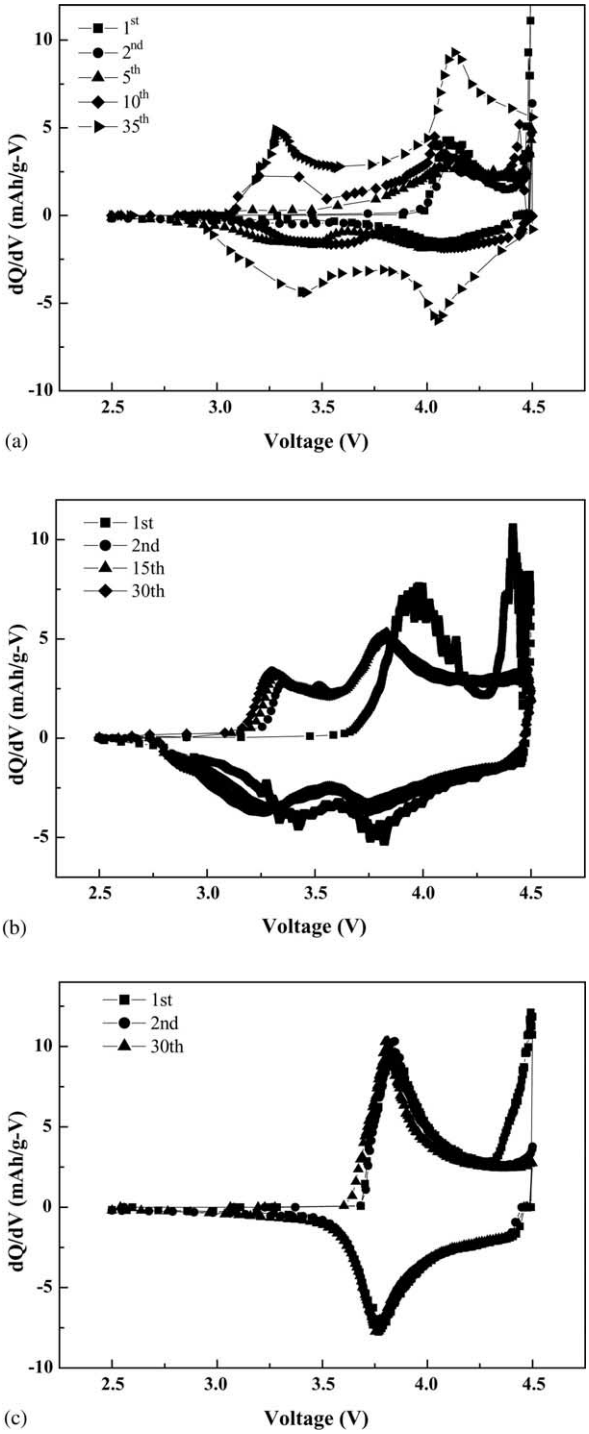

Fig. 5. Differential capacity vs. voltage for samples A–C.

for sample B than sample A. The increase of the reduction peak of manganese is also observed from the discharge process of samples A and B. The observation above indicates that not only Ni, but also Mn in samples A and B may contribute to the increase of discharge capacity of samples A and B. The growth of Mn oxidation peak with cycling seems to result in the increase of the discharge capacity of samples A and B at the initial cycle numbers, as shown in Fig. 5. The fast growth rate and larger area of the Mn oxidation peak results in faster saturation time and higher discharge capacity of sample B, respectively. On the other hand, the sample C has only one peak at 3.75 V, which is due to the reduction of Ni^{4+} to Ni^{2+}. After the first cycle, the oxidation and reduction are almost same in the shape for the first cycle except appearing irreversible peak at 4.46 V. This result suggests that only one phase might preserve during the oxidation and reductions processes, which indicates negligible structural degradation or transformation. Similar dQ/dV curves were also observed for samples D and E.

XRD data of Fig. 2a and b hint that the Mn in Li_2MnO_3 included as an impurity in as-synthesized samples A and B may participate in an electrochemical reaction during charge/discharge reactions, resulting in the production of the oxidation and reduction peaks in Fig. 5a and b. Sample C, which did not show the evolution of Li_2MnO_3 from its XRD spectrum, has only the reduction/oxidation peaks of nickel, as shown in Fig. 5c. At present, it is not clearly explained how the Mn in Li_2MnO_3 participates in the electrochemical reaction during charge/discharge processes. But we speculate that small amount of Li_2MnO_3 impurity existing in the as-prepared samples generates some defect, which instabilizes the layered $Li[(CoNi_{1/2}Mn_{1/2})_x(Li_{1/3}Mn_{2/3})_{(1-2x)}]O_2$ structure. Mn in the unstable structure can readily participate in an electrochemical reaction at a certain applied voltage, resulting in the evolution of nickel reduction/oxidation peaks. The increased cycle numbers seems to rearrange the atomic structure of unstable as-prepared samples to form a stable structure, leading to the stabilization of discharge capacity at certain cycle number, as observed from Fig. 5a and b.

4. Conclusion

Solid solutions with layered lithium manganese oxides, expressed with a design equation of $Li[Co_x(Li_{1/3}Mn_{2/3})_y(Ni_{1/2}Mn_{1/2})_{1-x-y}]O_2$, were synthesized using a triangle phase diagram proposed in our work. It was identified that the phase diagram is applicable for the designing new manganese oxides solid solutions. The synthesized manganese oxides solid solutions were synthesized with typical layered structure. The solid solutions were synthesized with maintaining the manganese oxidation state of 4+ and showed a one-step monotonous discharge curve shape without structural transformation to spinel during charge/discharge processes.

Acknowledgment

This work was supported by of the Ministry of Science and Technology (2004).

References

[1] P.G. Bruce, A.R. Armstrong, R.L. Gitzendanner, J. Mater. Chem. 9 (1999) 193.
[2] I.J. Davidson, R.J. McMillan, J.E. Greedan, J. Power Sources 54 (1995) 232.
[3] E. Rossen, C.D.W. Jones, J.R. Dahn, Solid State Ionics 57 (1992) 311.
[4] S.-S. Shin, Y.K. Sun, K. Amine, J. Power Sources 112 (2002) 634.
[5] T. Ohzuhu, Y. Makimura, Chem. Lett. 8 (2001) 744.
[6] J. Reed, G. Ceder, Electrochem. Solid State Lett. 5 (2002) A145.
[7] Z. Lu, D.D. MacNeil, J.R. Dahn, Electrochem. Solid State Lett. 4 (2001) A191.
[8] B. Ammundsen, J. Paulsen, I. Davidson, R.S. Liu, C.H. Shen, J.M. Chen, L.Y. Jang, J.F. Lee, J. Electrochem. Soc. 149 (2002) A431.
[9] T. Ohzuku, A. Ueda, M. Nagayama, Y. Iwakoshi, H. Komori, Electrochim. Acta 38 (1993) 1159.
[10] S.-H. Kang, J. Kim, M.E. Stoll, D. Abraham, Y.K. Sun, K. Amine, J. Power Sources 112 (2002) 41.
[11] Z. Lu, D.D. MacNeil, J.R. Dahn, Electrochem. Solid State Lett. 4 (2001) A200.
[12] S.J. Jin, K.S. Park, M.H. Cho, K.S. Nahm, The 44th Battery Symposium in Japan, Abstract 2A 16 Sakai, Japan, November 4–6, 2003.
[13] J.H. Kim, Y.K. Sun, J. Power Sources 119–121 (2003) 166.
[14] J.H. Kim, C.S. Yoon, Y.K. Sun, J. Electrochem. Soc. 150 (2003) A538.
[15] Z. Lu, J.R. Dahn, J. Electrochem. Soc. 149 (2002) A815.
[16] Z. Lu, J.R. Dahn, J. Electrochem. Soc. 149 (2002) A1454.
[17] S.H. Park, Y.-K. Sun, J. Power Sources 119 (2003) 161.